Kink Instabilities of the Post-Disruption Runaway Electron Beam at Low Safety Factor

C. Paz-Soldan[1], N. W. Eidietis[1], Y. Q. Liu[1], D. Shiraki[2], A. H. Boozer[3], E. M. Hollmann[4], C. C. Kim[5], and A. Lvovskiy,[6]

[1] General Atomics, P.O. Box 85608 San Diego, California 92186-5608, USA
[2] Oak Ridge National Laboratory, Oak Ridge, TN, USA
[3] Columbia University, New York, NY 10027, USA
[4] University of California-San Diego, La Jolla, CA 92093, USA
[5] SLS2 Consulting, San Diego, California 92107, USA
[6] Oak Ridge Associated Universities, Oak Ridge, Tennessee 37831, USA

Abstract. Realization of a high-current (approaching 1 MA) post-disruption runaway electron (RE) beam in DIII-D yields controlled access to very low edge safety factor (q_a) conditions. This enables unique observation and study of low-order kink instabilities in post-disruption plasmas where the current is carried entirely by relativistic REs. The conventional external kink stability boundary (in terms of q_a and internal inductance, ℓ_i) is found to accurately predict the operational space of the RE beam, with q_a limited to ≈ 2. Kink instabilities appear with a characteristic growth rate of a few tens of microseconds (which is comparable to the Alfven time) and ultimately cause complete loss of the RE population on a similar time-scale. This characteristic RE loss time is significantly faster than observations away from the $q_a \approx 2$ stability limit and implies both higher peak heat loading but also less chance of destructive magnetic to kinetic energy conversion via RE beam regeneration. With large enough kink amplitude no RE beam regeneration is observed, indicating the magnetic to kinetic energy conversion was inhibited. Instability structure analysis reveals that early instabilities at high q_a ($\gtrapprox 4$) are likely internal or resistive kinks (at higher poloidal mode number), while at $q_a \approx 2$ the most destructive instabilities are either internal or external kinks with low-order poloidal mode number ($m = 2$). The HXR loss magnitude is found to be proportional to the perturbed magnetic field and exhibits a helical spatial pattern. These observations are novel for present-day tokamaks yet will potentially be very common in high current tokamaks such as ITER, where predicted RE beam equilibrium evolutions cross the $q_a \approx 2$ stability boundary.

1. Introduction and Motivation

The risk of exciting high-current runaway electron (RE) beams becomes increasingly severe as the plasma current (I_P) of a tokamak increases. This is due to the exponential sensitivity of the RE avalanche multiplication process on I_P, which goes $\propto \exp(I_P[\mathrm{MA}]/0.4)$[1]. Considering the specific example of the ITER tokamak, its design I_P of 15 MA can amplify an initial RE seed current by a factor of e^{38}, which is $\mathcal{O}(10^{14})$ more amplification than a typical 2 MA DIII-D discharge (amplification factor of e^5). For this reason, the importance of addressing the RE problem to enable ITER to safely access its design I_P has been well-appreciated [2, 3, 4, 5]. A concentrated experimental and theoretical effort is underway to understand and mitigate RE effects for ITER using present-day tokamaks as experimental test-beds [6, 7, 8, 9, 10, 11, 12, 13, 14, 15, 16].

One aspect of the RE problem that has received remarkably little experimental and theoretical attention is the effect on RE dynamics of macroscopic MHD instability at high RE I_P and consequently low edge safety factor (q_a), specifically when $q_a \approx 2$. Due to the potential to transfer a large fraction of the pre-disruption I_P to the RE population in high I_P tokamaks, RE beams in devices such as ITER will be much more likely to traverse macroscopic MHD instability boundaries encountered at low q_a - namely the external, resistive, and internal kinks [17, 18, 19, 20, 21]. For example, simulations using the DINA code [22] reported in Ref. [23] self-consistently evolved ITER RE beam equilibria initialized with a variety of initial 'seed' RE current distributions which were then allowed to undergo avalanche multiplication. These studies found that most initial current distributions evolved to low q_a (< 2) and high internal inductance ($\ell_i > 1.3$) where instability might be expected based on experience from thermal (non-RE) plasmas. Separate theoretical studies of resistive instabilities of the RE beam were considered in Ref. [24], with the finding that the linear resistive instability behavior is approximately the same as a plasma without REs but with the same current profile.

The absence of controlled experimental data on this question can be appreciated by noting that REs pose operational risks even in present-day tokamaks. Thus, the maximum RE I_P is usually under strict administrative control to a level far below the operating non-RE I_P for a given device. Additionally, the weak avalanche amplification factor of present-day devices generally cause low I_P (few 100 kA) RE beams, and the available central solenoid flux is usually insufficient to increase I_P enough to access $q_a \approx 2$. These technical and administrative issues have prevented systematic experimental study of kink instability effects associated with $q_a \approx 2$ RE beam operation.

Indirect evidence for the kink instability impact on RE dynamics has also been proposed to explain some features of high-I_P RE loss cases in JET [9], where simple estimates found no q_a values below 2, possibly indicating the presence of kink instabilities. The final loss dynamics in Ref. [9] were suggested to be due to MHD instabilities, though no observation of instability or an associated interaction with the RE beam was presented. The interaction of lower I_P RE beams (0.25 MA) with the

first-wall in DIII-D was presented in detail in Ref. [25], presenting a useful reference point for the present study at much higher I_P and lower q_a.

Despite the scarcity of data, whether or not the RE beam is MHD stable is a fundamental question when considering RE mitigation, as is documenting and understanding the observed dynamics when the RE beam goes MHD unstable. MHD instabilities may abruptly terminate the RE beam before RE mitigation methods are applied, or alternatively MHD instabilities may significantly affect the RE beam evolution during mitigation. Owing to the large non-axisymmetry and potential for rapid stochastic transport, RE loss dynamics driven by macroscopic MHD may be very different from RE loss in more MHD stable situations [26, 27, 28, 29]. Finally, the operational boundaries identified using non-RE tokamak plasmas have not been experimentally shown to be accurate for relativistic RE beams. These open questions motivate the present study.

In this paper the observation and impact of macroscopic MHD instabilities at low q_a on the post-disruption RE beam is presented. The conventional stability boundary for the external kink is shown to accurately predict the operational range of the RE plateau, with the limiting instability appearing on an Alfvenic time-scale having a $m/n = 2/1$ structure consistent with internal or external kink modes with $q_a \lessapprox 2$. Higher-order and less virulent kink instabilities are also found at higher q_a ($\gtrapprox 4$), consistent with either resistive or internal kinks. Observed kink instabilities cause significant and ultimately total loss of the RE population on a time-scale similar to the mode growth (tens of microseconds). This fast time-scale forces re-evaluation of first-wall heating calculations and prevents regeneration of the RE beam and subsequent conversion of magnetic to kinetic energy. The RE loss spatial patterns are found to be distributed, helical, and with a toroidal phase related to that of the magnetic structure.

The structure of this paper is as follows. Experimental setup and basic observations are shown in Sec. 2. Equilibrium evolution towards instability is discussed in Sec. 3. The fast dynamics of the final loss are shown in Sec. 4. Magnetic analysis of the observed instabilities and comparison with ideal and resistive MHD simulation is presented in Sec. 5. Spatially-resolved measurements of the RE loss are given in Sec. 6. Discussions and conclusions are given in Sec. 7.

2. Experimental Setup and Basic Observations

As discussed in Sec. 1, regular operation of present-day tokamaks inhibits controlled access to the $q_a \approx 2$ RE regime. The simple path of reducing the toroidal field (B_T) has been reported to inhibit RE production [30, 31], thus it is not usually attempted. The alternate path of increasing RE beam I_P is challenging both due to administrative limits on the maximum allowable RE beam I_P, as well as the technical difficulty in raising I_P from generally low initial values to those needed to access $q_a \approx 2$. Both barriers to $q_a \approx 2$ RE beam operation were overcome in DIII-D discharge 177040, where the RE beam reached $I_P \approx 1$ MA and became repeatedly unstable to macroscopic MHD instability.

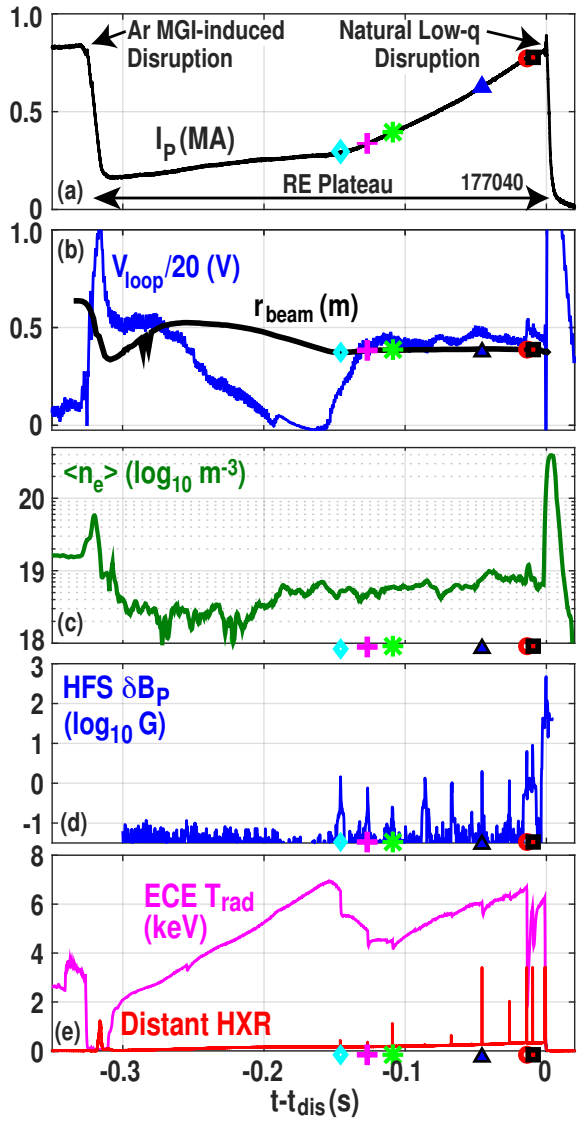

Figure 1. (color online) (a) Global evolution of high-I_P RE beam. Low safety factor is achieved by combination of high current (I_P), (b) slightly reduced beam radius (r_{beam}), high loop voltage (V_{loop}), and (c) fairly low $<n_e>$. Large-scale deconfinement events (colored symbols) are observed in (d) magnetic probe and (e) ECE, HXR signals.

As this I_P level is administratively prohibited, additional discharges of this type could not be requested and consequently the analysis in this work is limited to this singular discharge.

To reach this record high I_P value for a DIII-D RE beam, the plasma control system was programmed to maximize I_P, such that the central solenoid was delivering maximum loop voltage (V_{loop}). This enabled the imposed V_{loop} to eventually raise I_P to the required values approaching 1 MA, as shown in in Fig. 1(a). During this time the RE beam position is controlled using the standard DIII-D RE shape controller and is limited in size by the tokamak center post. A small programmed contraction of the RE beam minor radius (r_{beam}) also assisted in $q_a \approx 2$ access, shown in Fig. 1(b). This

also increases the B_T at the magnetic axis (from 2.1 to 2.5) and causes a transient drop in V_{loop}. Furthermore, deuterium (D_2) massive gas injection (MGI) significantly reduced the density [Fig. 1(c)] and resistivity of the RE beam through the unexplained mechanism first shown in Ref. [13]. It should be noted that while RE beam shape control is routine in DIII-D (as described in Ref. [32]), no such control capability is expected in ITER due to the comparatively slower control coil response times arising from the fact that the poloidal field coils are more distant and superconducting.

As I_P increased, large-scale MHD activity measured by magnetic probes begin to be observed [Fig. 1(d)] together with indications of RE loss. RE loss is evidenced by sudden drops in electron cyclotron emission (ECE) and sudden rises in hard X-ray (HXR) emission measured by a distant plastic scintillation detector [Fig. 1(e)]. ECE is here used as a proxy for the internal RE population, though ECE emission is weighted to few MeV energy and more perpendicular velocity orientation [33, 34]. The availability without cut-off of the ECE measurement as a proxy for the internal RE population is an important feature of this study, enabled by the low density condition of the RE beam after D_2 MGI.

The HXR detector scintillation signal measures bremsstrahlung emission from the RE beam, and is proportional to both HXR energy and quantity with uncertain weighting. It is also located several meters from the tokamak and tends to measure volume-integrated data. For this reason it is termed the distant HXR detector. Its measurement serves as a proxy for the total RE-induced bremsstrahlung emission. Signal spikes in this detector are used as a proxy for RE loss, since during the loss event the HXR emission is dominated by bremsstrahlung emitted by RE-wall interactions. The distant HXR also picks up emission from within the RE beam, as seen in the rising HXR baseline, though this part of the signal is small. Note the distant HXR spikes are often saturated, so no relative intensity information can be obtained from this measurement. Each loss event (burst) is indexed by a colored symbol, and this indexing will be used throughout this work when examining each loss event in detail.

Beyond the ECE and distant HXR measurements, Fig. 2 displays other instruments used in this study as well as the RE beam position and cross section. The beam major radius (R) and minor radius (r_{beam}) are 1.44 and 0.39 m respectively for the low q_a phase. Control of the RE beam position to the center of the tokamak enables accurate diagnosis of the instability spatial structure with toroidal arrays of magnetic probes (indicated in blue in Fig. 2) and HXR detectors (indicated in cyan in Fig. 2). Note a toroidal array of magnetic probes and HXR detectors exist at each indicated poloidal position. For the magnetics, arrays on the high-field side (HFS) consist of 8 independent probes per row, while arrays on the low-field side (LFS) have 8 probes for off-midplane rows and 10 probes for the midplane row [35]. HXR detector arrays consist of three detectors for each off-midplane row, and four detectors for the midplane row [36]. The HXR detector type is Bismuth-Germanium Oxide (BGO) for the toroidal arrays [37], while the distant HXR detector employs polyvinyltoluene Bicron BC-400 plastic scintillators [38].

Though this work focuses on the post-disruption RE beam phase, the pre-disruption

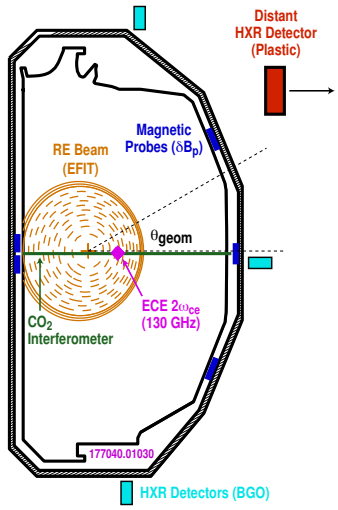

Figure 2. (color online) DIII-D tokamak cross section, indicating the location of the RE beam during the low q_a phase, as well as the diagnostics used in this study. Magnetic probes and BGO-based HXR detectors are actually several toroidally distributed measurements.

plasma scenario utilized is a low density, elongated, inner-wall limited plasma with B_T at the vessel center of 2.1 T, I_P = 0.8 MA. The plasma was heated by 2.1 MW of electron cyclotron heating aimed to the plasma core, yielding a peaked profile with core electron temperature (T_e) of 6 keV. The RE beam is initiated by the injection of a solid Argon pellet. This scenario is conventional for DIII-D RE experiments in all respects except for the somewhat reduced I_P, and is further described in Ref. [7]. It should also be noted that during the RE plateau phase (from $t - t_{\rm dis}$ = -0.33 s to -1.15 ms) I_P is overwhelmingly carried by the relativistic population. This can be most clearly seen by noting the bulk T_e is measured to be $\approx$ 1.5 eV using line ratio coronal estimates [39] implying a Spitzer resistivity of 5 mΩ, while as will be discussed the measured resistance is closer to 5 $\mu\Omega$. Thus, the current must overwhelmingly be carried by non-thermal REs to allow the observed low V_{loop}.

3. Equilibrium Evolution and Stability Boundary

Equilibrium reconstruction of the RE beam magnetic geometry allows comparison of stability boundaries developed for non-RE plasmas to those observed in the post-disruption RE beam. Figure 3 shows the evolution of the RE beam as the final limiting instability is approached (at $t = t_{\rm dis}$). As I_P is rising rapidly, well separated HXR bursts are observed together with drops in ECE [Fig. 3(b)], indicating RE loss events. ECE drops occur together with brief rises in the interferometer $<n_e>$ [Fig. 3(c)], indicating a brief transfer of some RE current into bulk thermal current [25], likely mediated by a momentary increase in the internal electric field. This is evidenced externally by a small momentary rise in V_{loop} from 9 to 11 V [Fig. 3(c)], indicating also a brief increase

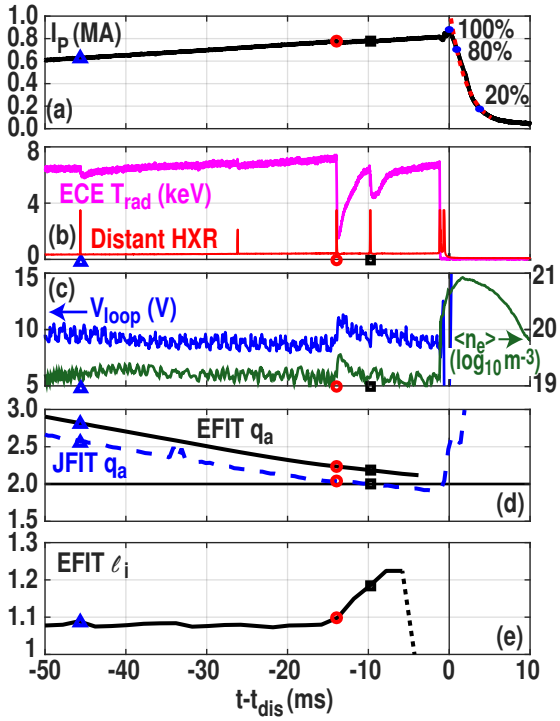

Figure 3. (color online) Trajectory of equilibrium parameters prior to the disruptive RE final loss event at $t_{\rm dis}$. (a) Plasma current (I_P), (b) distant HXR and ECE $T_{\rm rad}$, (c) V_{loop} and CO_2 interferometer $<n_e>$, (d) EFIT and JFIT calculations of q_a, and (e) EFIT-calculated ℓ_i.

of resistivity due to some of the current being momentarily carried by the thermal bulk. Note that on the short time scale (sub-ms) of the RE loss (ECE fall) the RE current cannot appreciably increase, necessitating the transfer to bulk current to conserve flux. On a longer time scale (5 ms), the current transfers back to the RE population and V_{loop} returns to nominal values.

$<n_e>$ also rises during this process because Ohmic power transfers from the RE beam to the bulk population, causing a momentary increase in ionization. Once the current returns to the RE population, this drive for ionization is removed, and the density falls back to the original level. It is interesting to note that during each burst the total I_P is nearly unchanged, indicating an efficient transfer of RE current to bulk thermal current during these loss events.

Two methods are used to compute the magnetic geometry. The first is the usual equilibrium code called EFIT [40], that solves the Grad-Shafranov equation assuming isotropic pressure. The experimental pressure is decidedly anisotropic, though as the pressure contribution to the Grad-Shafranov equation is small in these plasmas this may not be of consequence. A second method is provided by the JFIT code [41] which does not enforce the Grad-Shafranov equation but instead solves for a coarse grid of current elements within the vacuum vessel. This enables the code to run more robustly, especially during transient conditions.

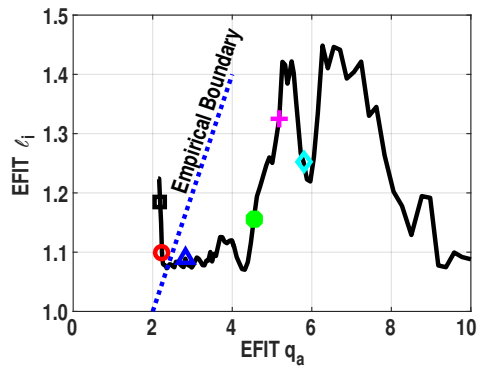

Figure 4. (color online) Evolution of RE equilibrium in kink stability space indexed by internal inductance (ℓ_i) and edge safety factor (q_a). Large loss events begin shortly after the empirical boundary from Ref. [44] is crossed, followed shortly thereafter by the final disruption.

Evaluation of the edge safety factor with EFIT and JFIT is shown in Fig. 3(d). A modest and systematic discrepancy is observed, with JFIT q_a lower than EFIT by about 0.2. The incomplete RE loss events prior to $t_{\rm dis}$ are well predicted by $q_a = 2$ with JFIT, although a few JFIT reconstructions just-prior to the final RE loss event (at $t_{\rm dis}$) indicate q_a slightly less than 2. EFIT values of q_a are slightly above 2 for the pre-disruptive loss events, while the final disruptive loss event at $t_{\rm dis}$ extrapolates closer to $q_a = 2$.

Considering the internal inductance (ℓ_i), it was found that the JFIT solution grid was too coarse to provide a useful ℓ_i value. EFIT-computed ℓ_i was calculable and is shown in Fig. 3(e). It has been previously shown that it is impossible to separate ℓ_i from the poloidal beta (β_p) in circular cross section tokamak equilibrium reconstructions, with the well-constrained parameter being $\beta_p + \ell_i/2$[42]. However, these plasmas are reconstructed to have an elongation of 1.1, which in the study of Ref. [42] were found to provide ℓ_i to within ≈10% using Solovev equilibria. This level of accuracy is deemed adequate for the present study.

The incomplete yet large-scale RE loss events prior to $t_{\rm dis}$ are found to lead to a significant rise in the computed ℓ_i. This indicates the RE current profile becomes significantly more peaked, as would be expected from the RE loss being preferentially driven at the edge of the RE beam. Interestingly, the RE I_P does not significantly change, so any loss of RE current (at the edge) was very rapidly replaced by new RE current (in the core). This process is thought to be mediated by changes in the internal electric field radial profile, though this is un-measured. These observations confirm the potential for RE regeneration in the event of incomplete RE loss events [43]. Ultimately, a complete RE loss without regeneration is observed for a sufficiently vigorous instability at $t_{\rm dis}$. After the complete RE loss, an I_P-spike and current quench (CQ) is observed, which will be further discussed in Sec. 4.

EFIT calculations of q_a and ℓ_i allow evaluation of the conventional tokamak operating space first discussed in Ref. [45] and compared to JET data in Ref. [44].

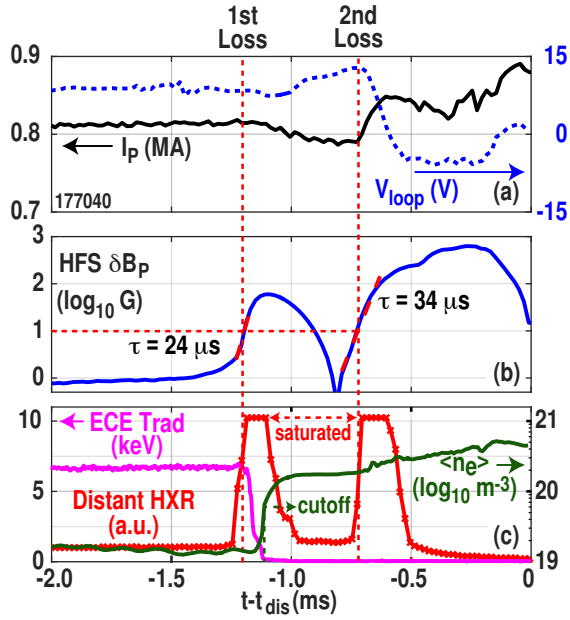

Figure 5. (color online) Fast dynamics of RE final loss in terms of (a) I_P (carried entirely by REs at -2.0 ms), loop voltage (V_{loop}), (b) HFS magnetic field (δB_p), and (c) ECE, HXR, and interferometer $<n_e>$ measurements.

The operating space is shown in Fig. 4, with the observed RE loss events indicated by the colored symbols (matching Fig. 1). The early RE beam evolution exists at considerably higher ℓ_i, favoring the excitation of internal kinks as will be described in Sec. 5. Nonetheless, it is clear that the empirical operating space boundary of Ref. [44] fairly accurately predicts the emergence of the major RE loss events, though less catastrophic loss events do occur in the stable region earlier in the evolution. The increase in ℓ_i observed after the major events only brings the RE equilibrium further into the unstable domain, until finally the RE beam is completely lost at $t_{\rm dis}$. Note EFIT reconstructions within a few ms of $t_{\rm dis}$ could not be converged, though JFIT indicates q_a continues to fall. The sudden drop in ℓ_i corresponds to the final converged EFIT reconstruction and is of unclear veracity.

4. Fast Dynamics at Final Loss

The fast-time scale dynamics associated with the complete RE loss event at $t_{\rm dis}$ and the subsequent current quench (CQ) are now considered. These measurements show microsecond timescales of both instability growth and RE loss, as well as the ability to fully lose the RE population without regeneration.

4.1. Complete RE Loss Event

Figure 5 presents high time-resolution measurements of final-loss dynamics for the narrowly-separated catastrophic RE loss events that ultimately trigger a thermal

quench-like event, complete with I_P-spike and subsequent CQ. What differentiates this event from those prior is clearly the magnitude of δB_p, which as shown in Fig. 1(c) exceeds the previous bursts by at least an order of magnitude. Even before δB_p reaches this high level, significant HXR loss is observed, with the distant HXR detector saturating at about $\delta B_p = 10$ G, and shortly thereafter the internal ECE measurement indicates the vast majority of the RE content within the beam is lost at $t - t_{\rm dis}$ = -1.15 ms. Shortly after the ECE signal is lost, the interferometer $<n_e>$ rises dramatically, indicating significant transfer of RE current into bulk thermal current starting at $t - t_{\rm dis}$ = -1.15 ms. After this time, as indicated by a dashed line in Fig. 5(c), no signal from the ECE system is expected due to right-hand ECE cutoff (estimated assuming a linear density profile).

After the first loss event, δB_p subsides prior to growing again and initiating a second loss event as evidenced by a second large HXR burst. It is speculated that the RE population partially regenerated between this first and second loss event, but with ECE in cut-off no internal verification is possible. After the second burst, no further HXR signal is observed, indicating the RE population has been completely lost. The presence of an I_P-spike at this time suggests fully open flux surfaces and rapid internal current re-arrangement, reminiscent of a thermal quench. Likely due to the presence of open field lines from the extremely large δB_p, no RE regeneration is observed, and the expected transfer of magnetic to kinetic energy does not take place.

These fast dynamics are rather different than what is observed in the high q_a ($\gtrapprox 4$) loss events described in Ref. [25]. Here, the entire RE population is lost in a few isolated HXR bursts, whereas at high q_a a multitude of repetitive and smaller loss events slowly degrade the RE current over ≈ 5 ms. This time-scale was found in Ref. [25] to correspond to the avalanche time. In this $q_a \approx 2$ regime, complete RE loss occurs within the Alfvenic time-scale of the MHD growth, which is about 100 μs.

The RE loss time-scale is an essential empirical input to first-principles predictions of the first-wall Joule heating from the RE loss [46]. Very different time-scales are clearly needed to treat MHD-stable RE beams at high q_a as compared to kink-unstable RE beams at $q_a \approx 2$. The faster loss of REs is undesirable as it will lead to increased first-wall heating, as there is less time for heat to dissipate via radiation or conduction.

4.2. Current Quench

A second parameter necessary to estimate the impact of the disruption is the time-scale associated with the current quench (CQ). It is experimentally unknown whether the CQ timescale or dynamics would be different for a $q_a \approx 2$ instability of the RE beam as compared to non-RE plasmas. In this Section the CQ time is measured and shown to be consistent with the inductive current decay assuming the entire RE current transferred to the cold (few-eV) bulk electron population. The CQ is thus found to be entirely conventional despite its unusual origin.

The experimental CQ dynamic is shown in Fig. 3(a) alongside an exponential fit

to the I_P trace and marked time-points where the current is at 100%, 80%, and 20% of the maximum value. The time between the 100% and 80% value is 0.95 ms, and between the 80% and 20% value is 2.8 ms. These values fall right in the middle of a wide ensemble of DIII-D CQ time-scales, indicating they are not anomalous for DIII-D [47]. The exponential fit yields an inductive L/R decay time ($\tau_{L/R} = L/R$) of 2.1 ms, where L is the inductance and R is the resistance.

The observed $\tau_{L/R}$ can be compared to expectations based on estimates of L and R taken before the final loss events begin. This is done in order to infer whether the beam R is appreciably larger during the CQ than before the final loss, which if true supports the hypothesis that the entire RE current transfers to the thermal bulk during the final loss event. To achieve this, a simple L/R circuit equation ($V_{loop} = L(dI_P/dt) + RI_P$) is applied to the time before the loss events begin in Fig. 5, where measured values of $V_{loop} = 9$ V, $I_P = 0.8$ MA, and $(dI_P/dt) = 3.5$ MA/s are obtained.

A first estimate of L taken from Eq. 4 in Ref. [43] yields $L = 3.6\ \mu H$. Surprisingly, using this estimate of L in the circuit equation implies $L(dI_P/dt) > V_{loop}$, which is unphysical. This constraint provides a firm upper bound of $L < V_{loop}/(dI_P/dt)) = 2.6$ μH. An estimate of R can be obtained from similar D_2-dominated RE discharges reported in Ref. [13], where in contrast to this discharge $I_P/dt = 0$. This yields R in the range of 5-8 $\mu\Omega$. Using this estimate of R in the circuit equation to compute L, a range of $L = 1.0$-$1.5\ \mu H$ is obtained. This range gives an expected $\tau_{L/R}$ in the range of 125-300 ms, which is two orders of magnitude slower than observed. This supports the conclusion that the current is no longer carried by the collisionless (and thus low R) RE population but rather by colder and more resistive bulk electrons.

A further verification of cold bulk T_e during the CQ is possible by assuming L is unchanged through the final loss and I_P-spike, and using the observed $\tau_{L/R}$ to infer R. Using Spitzer resistivity, R can then be used to calculate the bulk T_e. These calculations are rough as mutual inductance effects during the CQ are ignored, as are possible changes in the internal current profile changing L through the final loss and I_P-spike. Using the initial L (1.0-1.5 μH) with the observed $\tau_{L/R}$ (2.1 ms) yields $R =$ 0.5-0.7 mΩ. Using Spitzer resitivity (taking $Z = 1$) this yields T_e is 5-7 eV, which is firmly not relativistic. These observations support the conclusion that the entire RE population was lost through the I_p-spike, giving rise to a conventional CQ.

5. Kink Instability Magnetic Structure and Model Comparison

Each magnetic burst and RE loss event highlighted in Fig. 1 is now attempted to be identified with its underlying magnetic instability. This is done by measuring the toroidal and poloidal structure with the magnetic probe array and comparing it to predictions from ideal and resistive MHD modeling using the MARS-F code [48]. This experiment-model comparison will reveal the possible importance of several types of instabilities, namely the resistive, internal, and external kinks. The first two (resistive, internal) will be shown to be consistent with measurement at high q_a ($\gtrapprox 4$), while the

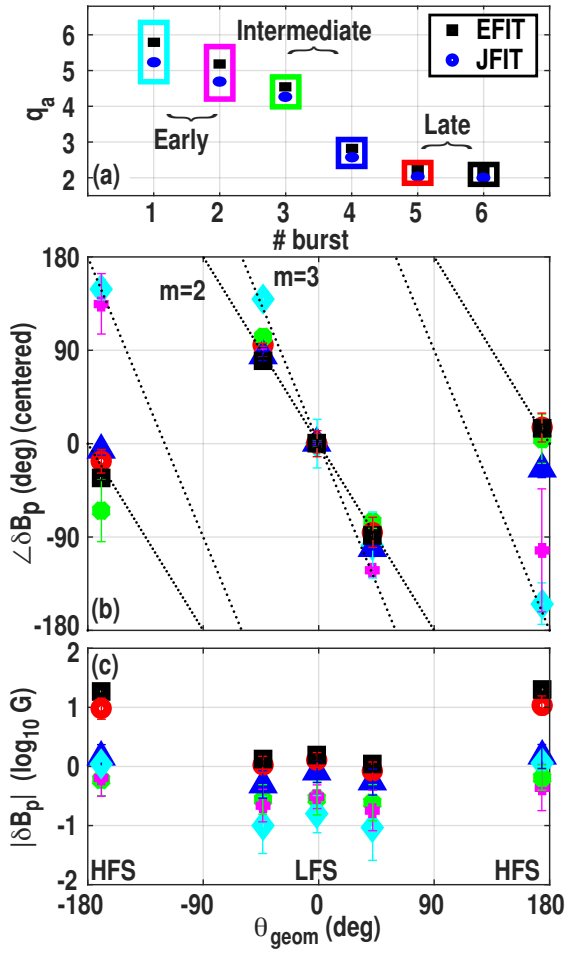

Figure 6. (color online) (a) q_a value and color coding, (b) toroidal phase, and (c) amplitude of the $n = 1$ component of the poloidal magnetic field (δB_p) measured on the probe arrays shown in Fig. 2. Measurements are averaged for the peak 0.1 ms of the rapid bursts associated with each RE loss events, with color coding matching Fig. 1. Error bars are taken as the standard deviation of the measurement over the 0.1 ms burst period. For clarity, the absolute toroidal phase is shifted such that the LFS phase is 0 degrees. The expected helicity of a single $m = 2$ and $m = 3$ perturbation is also shown.

latter two (internal, external) are consistent with measurement at $q_a \approx 2$.

5.1. Experimental Mode Structures

Spatially distributed magnetic probes allow determination of the toroidal and poloidal mode numbers associated with the RE loss events highlighted in Fig. 1. Toroidal resolution clearly identifies the toroidal structure to be overwhelmingly $n = 1$ in all cases. Poloidal resolution is provided by separate toroidal arrays at five different θ_{geom}, as shown in Fig. 2. Note only the poloidal magnetic field (δB_p) is considered as the MHD activity is so rapid that the radial magnetic field is strongly shielded by the conducting vacuum vessel. Results of the magnetic modal analysis are shown in Fig. 6. Colors are

coded to the symbols found in Fig. 2, one color per RE loss event, and the q_a values are shown in Fig. 6(a). The final disruptive burst discussed in Sec. 4 is not included in the analysis as it quickly saturates several magnetic probes. However, data early in the growth phase of this final instability reveals its structure to be essentially identical to the two penultimate bursts (red circle, black square) at similarly low values of q_a.

Considering the poloidal mode structure shown in Fig. 6(b), coherent phase information is found for each burst and the uncertainty is taken as the standard deviation of the phase within the 0.1 ms burst period. Even and odd poloidal structures are clearly identified by comparing the phase difference between the LFS and HFS midplane sensors, with in-phase structures called even and out-of-phase structures called odd. The helicity of the late bursts (green asterisk, blue triangle, red circle, black square) are consistent with an $m/n = 2/1$ (even) structure, while the earlier bursts (cyan diamond, magenta cross) are consistent with an 3/1 (odd) mode structure. This indicates that the early bursts, occurring at higher q_a ($\gtrapprox 4$), are of a different nature than the late bursts at $q_a \approx 2$.

Amplitude as a function of θ_{geom} is shown in Fig. 6(c). A much larger magnetic signal is always found on the HFS arrays, due to the simple fact that the RE beam is resting on the tokamak center-post and is thus nearer to the HFS arrays. The HFS/LFS ratio is between 2-10 and varies with each burst. These observations will now be interpreted with MHD modeling to try and identify the underlying MHD instabilities responsible for each burst, with model comparison results eventually summarized in Table 2.

5.2. Comparison to MARS-F Modeling

Two equilibria are generated using the EFIT code for ideal and resistive MHD analysis with the MARS-F code [48], one at $t - t_{\rm dis} = 150$ ms with $q_a = 6.04$ and a second at $t - t_{\rm dis} = 10$ ms with $q_a = 2.1$. Calculations include effects from the DIII-D resistive wall, though these are found to be weak. For resistive analysis, a resistive time (τ_r) of 2.5 ms is chosen, corresponding to the resistivity of the bulk (few eV) electrons as found in Sec. 4.2. This yields a Lundquist number ($S = \tau_r/\tau_A$) of $S = 10^4$. Note no treatment of the relativistic population is attempted in these simulations. The pressure is taken to be anisotropic, ignoring any anisotropic pressure from the predominantly parallel-directed REs. Resistivity is taken to be that of the bulk. The fluid model is thus essentially applied to the bulk plasma, but not the relativistic population. This is deemed to be a reasonable starting point, although as discussed in Sec. 7.2 future work can attempt to use a more self-consistent equilibrium model including the (small) relativistic population, both in the pressure tensor and the resistivity. A likely more important issue for this analysis is the lack of internal current profile constraints in the equilibrium fitting. Specifically, the on-axis safety factor (q_0) is not measured.

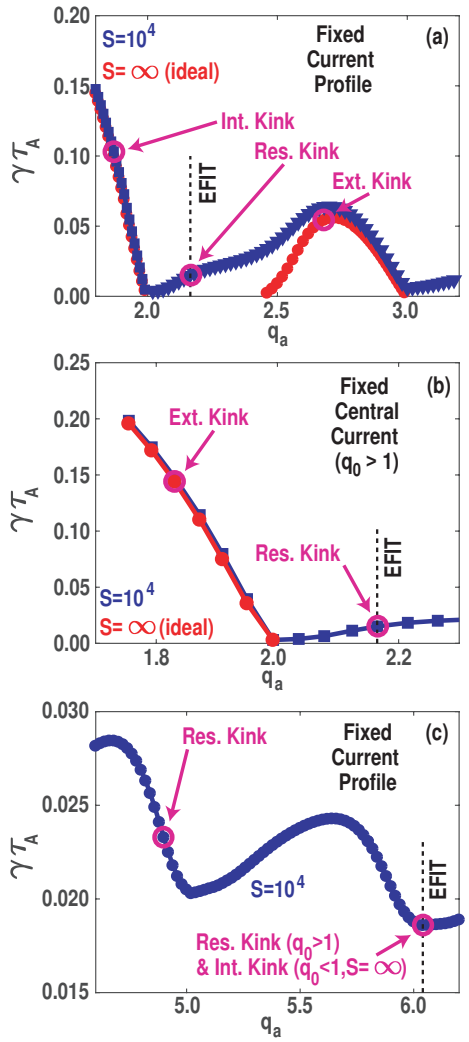

Figure 7. (color online) MARS-F computed instability growth rates for (a) the q_a = 2.1 equilibrium as q_a and q_0 are both varied, (b) the q_a = 2.1 equilibrium as only q_a is varied, and (c) the q_a=6 equilibrium as q_a and q_0 are both varied. Candidate instabilities for experimental mode structure comparison are identified and listed in Table 1.

5.2.1. Instability Space and Growth Rates To explore the various candidate instabilities numerical scans of the current profile are executed, as shown in Fig. 7. The computed instability growth rates (γ) are normalized to the Alfven time ($\tau_A \approx 0.25$ μs). The predicted growth rates are thus very rapid: $\mathcal{O}(10^5)$ s^{-1}. The observed instabilities are a textbook-like tour of ideal-resistive MHD, but are nonetheless here briefly reviewed for the benefit of the reader. Highlighted instabilities are also summarized in Table 1.

Without any modification of the input $q_a = 2.1$ equilibrium, instability is found at the experimental resistivity ($S = 10^4$). This instability is denoted the Resistive Kink, and its growth rate decreases with S by a power law [21]. At a conductivity far exceeding the experimental value ($S = 10^7$) the resistive kink becomes a dominantly tearing-type instability. Since this value of S is unphysical and the tearing mode grows far too slowly

Name	q_a	q_0	S	$\gamma\tau_A$
Internal Kink ($q_a \approx 2$)	1.85	0.97	∞	0.105
External Kink ($q_a \approx 2$)	1.83	1.13	∞	0.14
Resistive Kink ($q_a \approx 2$)	2.16	1.13	10^4	0.015
Tearing Mode ($q_a \approx 2$)	2.16	1.13	10^7	0.001
Resistive Kink (mid q_a)	4.8	1.5	10^4	0.023
External Kink (mid q_a)	2.7	1.4	∞	0.055
Resistive Kink ($q_a \approx 6$)	6.04	1.83	10^4	0.02
Internal Kink ($q_a \approx 6$)	6.1	0.97	∞	0.008

Table 1. Instabilities highlighted in MARS-F current profile scans that will be later compared to experimental measurements. Except in the tearing mode case, naming convention relates to q_0 (internal vs. external) and S (resistive or not). Instabilities with $S = \infty$ are by definition ideal though for brvity it is omitted from the name.

compared to experiment, it is excluded from further consideration.

Scanning the current profile self-similarly causes both q_a and q_0 to decrease. When q_0 drops below one (alongside q_a below two), a strongly growing instability is found and is denoted the Internal Kink [Fig. 7(a)]. It is ideally unstable, in that it is unchanged by taking $S \to \infty$. To avoid the internal kink, a second scan of q_a (from 1.7 to 2.3) while fixing $q_0 > 1$ is executed, with the ideal External Kink found when q_a drops below two [Fig. 7(b)]. The internal and external kinks have very similar growth rates but are differentiated by their mode structure, dominantly $m/n = 1/1$ in the internal case and both 1/1 and 2/1 in the external case.

Considering the $q_a \approx 6$ equilibria [Fig. 7(c)], no ideal instability is found when q_a drops below the integer 6. The experimental S is however unstable to a resistive kink at this q_a value. Reducing q_0 below one in this equilibrium again destabilizes the ideal internal kink, this time at much higher q_a. Continuing to reduce q_a traces the usual undulating growth rate pattern with integer q_a, and a slightly lower q_a (≈ 5) resistive kink is highlighted for comparison to intermediate q_a experimental cases.

5.2.2. Model-Experiment Comparison: Poloidal Structure and Growth Rates The instabilities identified in Fig. 7 are now compared to the experimental measurements shown in Fig. 6. The bursts early in time are compared to the $q_a \approx 6$ equilibrium results [Fig. 8(a,b)], intermediate time bursts are compared to a mix of both equilibrium results [Fig. 8(c,d)], and late time bursts are compared to the $q_a \approx 2$ equilibrium results [Fig. 8(e,f)]. As the MARS-F stability calculations returns only the relative amplitude, the amplitudes are normalized to measurements on the HFS (with a confidence interval), and the phase is shifted to match the observed LFS midplane ($\theta_{geom} = 0$) phase. Uncertainties are propagated in both the experimental data points and the normalization of the predicted amplitude structure to the HFS amplitude.

A broad conclusion is that despite the fact that the relativistic population is ignored

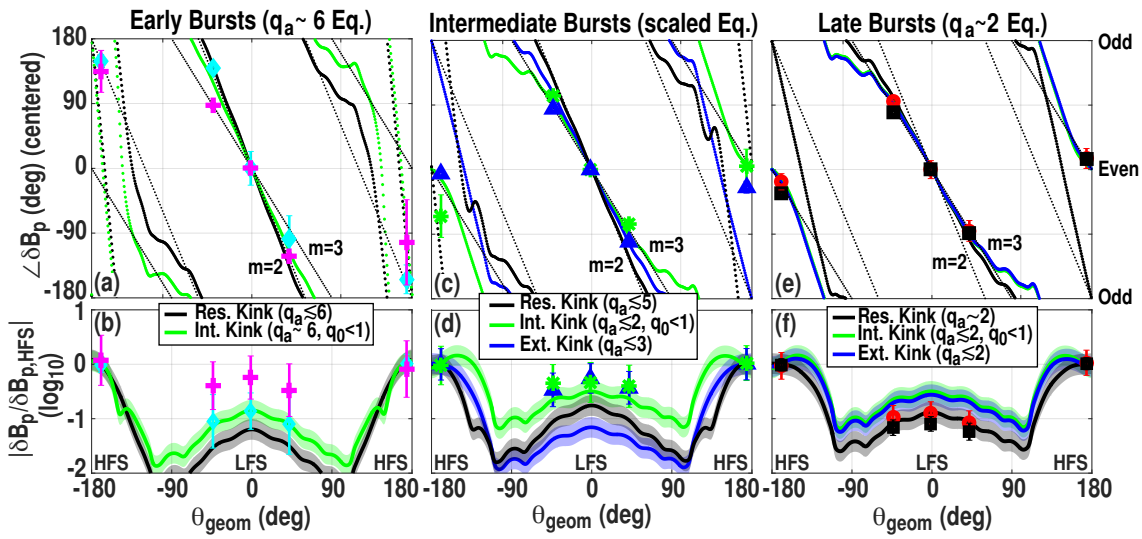

Figure 8. (color online) Comparison of MARS-F predicted magnetic structure to experimental observation in terms of δB_p phase and amplitude for the (a,b) early bursts with the $q_a \approx 6$ equilibrium, (c,d) intermediate bursts with both equilibria, and (e,f) late bursts with the $q_a \approx 2$ equilibria. Dotted lines indicate rigid $m = 2$ and $m = 3$ helicity. Experimental datapoint colors are the same as previous figures and identified in Table 2.

in calculation, the MARS-F predicted mode structures are comparable to experimental measurements, enabling an effort to identify candidate instabilities by their magnetic mode structure. The two main features used to identify the instabilities is firstly whether the mode structure is even or odd (phase difference between LFS and HFS measurements) and secondly the ratio of the HFS to LFS amplitude. Due to the similarity between candidate instability mode structures, in many cases the external magnetic mode structure measurement cannot differentiate between the candidate instabilities, though some options can be excluded. Results are summarized in Table 2 and are now explained for each q_a range in turn.

Considering the early burst candidate instabilities in Figs. 8(a,b), the resistive kink and internal kink appear very similar in mode structure. This is expected, as the main difference is the destabilization of a core 1/1 component that couples weakly to the external magnetics. For both candidates, the phase dependence is odd helicity overall and has $m = 3$ helicity on the LFS, and both are consistent with experiment. Interestingly, the large experimental phase variation (large error bars) of the magenta points are consistent with the computed sensitive phase structure on the HFS. Amplitude comparison is shown in Fig. 8(b). A small distinction between the internal and resistive kink is found in the ratio of HFS and LFS amplitudes, with the data in better agreement with the internal kink. However, large uncertainty on the cyan data points prevent conclusive discrimination between the internal and resistive kink.

Intermediate q_a bursts are now compared in Figs. 8(c,d). The observed mode helicity is now even, while the external kink at $q_a \approx 3$ is odd. This excludes the q_a

color symbol	q_a	even/odd	$\lvert B_{HFS}/B_{LFS}\rvert$	$\gamma\tau_A$	Candidate Instabilities
cyan diamond	≈ 6	odd	≈ 10	0.018	Int. or Res. Kink
magenta cross	≈ 5	odd	≈ 2	0.010	Int. Kink
green asterisk	≈ 4	even	≈ 2	0.021	Int. or Res. Kink
blue triangle	≈ 3	even	≈ 2	0.008	Int. or Res. Kink
red circle	≈ 2	even	≈ 10	0.013	Int. or Ext. Kink
black square	≈ 2	even	≈ 10	0.013	Int. or Ext. Kink

Table 2. Experimentally measured δB_p mode structure, growth rate, and proposed candidate instabilities for bursts shown in Figs. 1 and 3 (with consistent color coding).

$\approx$ 3 burst (blue triangles) from being an external kink. For the same reason, the resistive kink at $q_a = 5$ is a poor match. This is either because the experimental q_a of these bursts ($\approx$ 3, 4) is lower, or because the observed instability is an internal kink. Considering the amplitude dependence, the internal kink is found to agree very well with the observations in both amplitude and phase, though the resistive kink is also within experimental uncertainty.

Finally, the late burst instabilities compared in Figs. 8(e,f). The phase of the data are of very similar helicity and are consistent with either the internal or external kink, while the resistive kink is excluded. The amplitude dependence indicates a small LFS/HFS ratio, actually consistent with all three considered instabilities found at q_a $\approx$ 2. Combining phase and amplitude, the most consistent instabilities are the internal and external kink, which recall are difficult to distinguish due to the weak coupling of the 1/1 component with external magnetics.

While the preceding discussion has focused on mode structure comparisons, the growth rate of each burst is also measured (shown in Table 2) and is always found to be a few tens of microseconds. For the experimental Alfven time (τ_A) of 0.25 μs, this gives $\gamma\tau_A$ of between 0.01-0.02. This timescale is Alfvenic, although slower than predictions for the ideal instabilities in Table 1. Due to the similarity of the growth times for each burst, the growth rate does not provide further relative discrimination between instabilities, except to generally favor the resistive kinks as their growth rates are generally slower. Further discussion of growth rate discrepancies are left to Sec. 7.2.

In summary, the mode structure comparison has thus highlighted that the observed mode structures vary with q_a, as do the most likely candidate instabilities. For early bursts at high q_a, internal or resistive kinks are implicated, while for late bursts the most likely instability is either the internal or external kink (with $q_a \lessapprox 2$). Experimental growth rates appear systematically lower (more stable) than model predictions.

6. RE Loss due to Kink Instabilities

In this final section an examination of the relationship between the magnetic mode structure and resultant HXR loss is conducted, utilizing the spatially distributed HXR

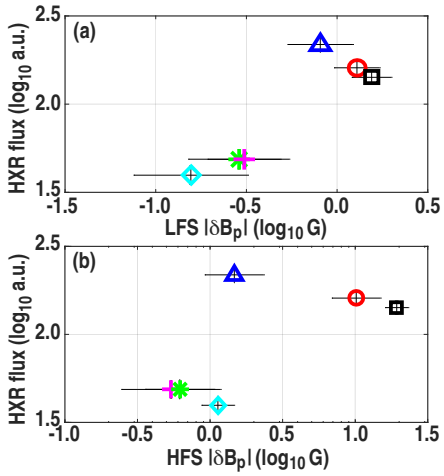

Figure 9. (color online) Relationship between the total integrated HXR flux summed over all detectors as compared to the magnitude of the (a) LFS δB_p and (b) HFS δB_p. HXR flux is integrated over the duration of each burst whose identity is given by the color code shown in Table. 2.

sensor arrays presented in Sec. 2. This will reveal a correlation between the magnitude the LFS δB_p with the total HXR flux as well as a helical HXR loss pattern whose toroidal phase (ϕ_{tor}) is related to the toroidal phase of the magnetic mode structure.

A relationship between the amount of flux registered on the spatial HXR arrays and the magnitude of the magnetic field during each burst is found, as shown in Fig. 9. HXR flux measurements are integrated over the entire spatial array and over the duration of each fast burst, while magnetic signals are processed as discussed in Sec. 5. A clear correlation is found between the magnitude of the LFS magnetic signal and the integrated HXR flux, but interestingly the correlation is poorer with the HFS sensors. This is surprising because the measured magnetic signals on the LFS are 2-10x smaller than on the HFS due to geometric effects. It can thus be concluded that the mode structure is important when considering the HXR loss. This observation may be due to a preferential loss of REs to the LFS of the device due to drift orbit effects that shift the RE orbits to the LFS of the corresponding flux surface. Dedicated simulations considering RE loss in the predicted non-axisymmetric fields from each instability class are required to further explore these correlations.

Final consideration is given to the spatial distribution of HXR emission originating from lost REs striking the tokamak wall. Figure 10 displays the spatial HXR loss pattern for each considered magnetic burst of this study, with each burst normalized to the maximum flux of each event. The spatial pattern varies between bursts. Early bursts are found to be localized to a single HXR detector, while later (and larger) bursts are more distributed, registering more flux above and below the midplane. Interestingly, the larger bursts are consistent with the helicity of the observed magnetic mode. Finally, the toroidal phase (ϕ_{tor}) of the magnetic structure is related to the toroidal phase of

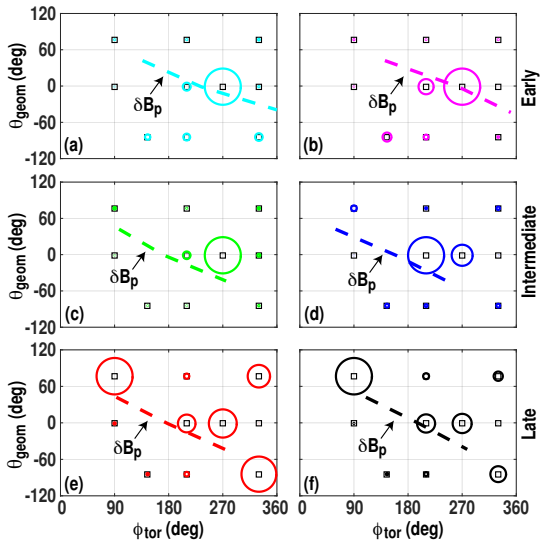

Figure 10. (color online) Spatial plot of HXR flux as registered by the spatial array, where each circle centroid is the location of the BGO scintillator in θ_{geom} and toroidal phase (ϕ_{tor}) and the size of the circle is proportional to the relative flux registered at that point during each burst. Midplane BGOs dominate the emission and are thus scaled down by 5x. The dashed line indicates the measured δB_p maximum to the tokamak LFS wall. Each panel corresponds to a specific HXR burst event with the color coding in Table. 2.

the measured HXR flux. This further reinforces the connection between the RE loss pattern and the underlying structure of the observed instability.

7. Discussion and Conclusions

Novel experimental observations of RE beam instability at $q_a \approx 2$ provide needed input to model multi-MA I_P RE scenarios in future tokamaks such as ITER. In this Section observations are summarized, discrepancies with MHD modeling discussed, and implications of crossing the $q_a \approx 2$ stability boundary presented.

7.1. Summary of Results

The conventional tokamak stability boundary to the external kink is found to be accurate for RE beams, with conventional 2/1 internal or external kinks found to be the limiting instability at $q_a \approx 2$. This indicates that any predicted post-disruption equilibrium trajectory that crosses this boundary must account for the instability dynamics presented in this work.

Near the stability boundary, magnetic probes reveal large-magnitude kink instabilities that cause severe and repeated RE loss events. With large enough kink amplitude the entire RE population is lost. With complete RE loss no RE beam regeneration is observed, indicating that magnetic to kinetic energy conversion was inhibited. This offers possible advantages for RE mitigation, as will be described in

Sec. 7.3. After complete RE loss, the subsequent current quench time is consistent with a conventional inductive decay of the current, now carried by few-eV background electrons.

Prior to the complete final loss, large-scale kink instabilities also dump significant amounts of REs, with magnetic mode structure comparisons to MHD modeling indicating the candidate instabilities are either internal or resistive kinks at high q_a ($\gtrapprox 4$) and either internal or external kinks at $q_a \approx 2$. During these events, the RE loss pattern (measured via HXR emission) is found to be distributed and helical in nature, as expected from the large-scale and helical δB produced by the various kink instabilities. This suggests a mechanism whereby the magnetic surfaces break up as a result of the large scale δB and make direct contact along the field-line with the wall. Field-lines with pre-existing intersections with the wall, populated with REs by the large δB, thus form a circuit to dump the REs to the wall. This evidently happens over a large spatial extent due to the global nature of the kink δB field. Interestingly, despite the near-MA level RE current at the final loss, no unusual damage to the DIII-D first wall was found. This may also be due to the more spatially distributed nature of the RE loss at $q_a \approx 2$.

These observations provides novel empirical input to calculate the RE final loss and CQ dynamics at $q_a \approx 2$. Both the δB growth and the RE loss are found to take place on a tens of microsecond (Alfvenic) time-scale, which is orders of magnitude faster than observed in higher q_a (more MHD-stable) conditions [49]. This faster time-scale can be used to better predict the first-wall Joule heating from the RE loss at $q_a \approx 2$ [46]. Interestingly, it is debatable whether the $q_a \approx 2$ situation is advantageous as compared to the higher q_a situation, as will be discussed in Sec. 7.3.

Finally, further experimental exploration and improved statistics on the reported phenomena is clearly desirable and would benefit from more discharges of the type reported in this work. However, a substantial increase in the maximum allowable RE I_P on DIII-D would be required to achieve this and is not foreseen.

7.2. Open Questions from MHD Modeling

Comparison of experiment to MHD modeling finds that the observed growth rates are systematically lower than model expectations, and that resistive instability is predicted for all low q_a despite the discrete (burst-like) nature of the experimental instabilities. These discrepancies indicate additional stabilization effects are needed to match the experiment. One possibility is that there is a stabilizing influence of the trapped REs on the kink instability [50], which is not treated. A second possibility is that coupling to halo currents slows the growth of the mode. A third possibility is that in analogy to the slow crossing of the beta-limit studied in Ref. [51], the instability growth time is slowed by the relatively gradual crossing of the marginal stability threshold. These possible explanations require further modeling to be isolated. Additional stabilizing effects are also needed to match the discrete nature of the experimental instabilities, as MARS-F predicts continual instability at low q_a for experimental values of resistivity (S).

Inclusion of the RE population in a kinetic MHD formalism would allow more conclusive comparison of the observed instability growth rates and is a subject for future work.

7.3. Kink Instability: Good or Bad for RE Mitigation?

Attention is now paid to the question of whether the appearance of a violent kink that causes a sudden and complete loss of the RE population is desirable. Naturally, when contrasting this situation with a controlled dissipation of the RE to very low currents without wall contact, a violent kink appears rather undesirable. However, comparing to an incomplete (wall-contacting) yet MHD stable RE dissipation, some advantages may appear. First, the global nature of the large deconfining δB may give rise to significantly larger RE wetted areas, in contrast to the very local interaction regions often observed [9]. This is supported by the wide spatial pattern of HXR loss discussed in Sec. 6. Second, the conversion of magnetic to kinetic energy expected as the RE comes into contact with the first-wall may be avoided if REs are fully deconfined by a large δB. This can occur because the large δB dumps the entire RE population, avoiding the repeated re-generation of REs expected if only a fraction of the RE population scrapes off on the first wall [43]. Since magnetic to kinetic energy conversion can significantly amplify the damage to the tokamak first-wall, this is a potentially significant advantage. Considering the tokamak nuclear operating phase however, the continual presence of RE seeds from tritium decay and wall-emitted gamma-rays would need to be considered as they could potentially re-seed the RE population [29] after a total loss event.

In this experiment, the picture is mixed - no re-generation is observed after the complete RE loss event at t_{dis}, though the earlier incomplete RE loss events did regenerate the lost RE population, likely converting some magnetic energy into kinetic. Finally, it should be noted that post-mortem and in-situ analysis did not reveal any damage to the DIII-D carbon wall during this near-MA level I_P RE strike, despite it carrying comparable I_P to strikes that have caused severe beryllium first-wall melting on JET [9] - though naturally the first-wall material is of crucial importance as well. Evidently, more modeling work is needed to quantitatively assess the benefits and drawbacks of crossing the $q_a \approx 2$ stability boundary.

Acknowledgments

This work is supported by Department of Energy grants DE-FC02-04ER54698, DE-AC05-00OR22725, DE-FG02-07ER54917, and DE-SC0016268. The authors wish to thank J. Herfindal, C. Lasnier, R. Moyer, D. Rudakov and E. Strait for operational and diagnostic support. This material is based upon work supported by the U.S. Department of Energy, Office of Science, Office of Fusion Energy Sciences, using the DIII-D National Fusion Facility, a DOE Office of Science user facility, under Awards DE-FC02-04ER54698. DIII-D data shown in this paper can be obtained in digital format by following the links at `https://fusion.gat.com/global/D3D_DMP`. Disclaimer: This

report was prepared as an account of work sponsored by an agency of the United States Government. Neither the United States Government nor any agency thereof, nor any of their employees, makes any warranty, express or implied, or assumes any legal liability or responsibility for the accuracy, completeness, or usefulness of any information, apparatus, product, or process disclosed, or represents that its use would not infringe privately owned rights. Reference herein to any specific commercial product, process, or service by trade name, trademark, manufacturer, or otherwise does not necessarily constitute or imply its endorsement, recommendation, or favoring by the United States Government or any agency thereof. The views and opinions of authors expressed herein do not necessarily state or reflect those of the United States Government or any agency thereof.

References

[1] Rosenbluth M N and Putvinski S V 1997 *Nuclear Fusion* **37** 1355 URL `http://iopscience.iop.org/0029-5515/37/10/I03`

[2] Hender T C, Wesley J C, Bialek J M, Bondeson A, Boozer A H, Buttery R J, Garofalo A M, Goodman T P, Granetz R S, Gribov Y, Gruber O, Gryaznevich M P, Giruzzi G, Günter S, Hayashi N, Helander P, Hegna C C, Howell D F, Humphreys D A, Huysmans G T A, Hyatt A W, Isayama A, Jardin S C, Kawano Y, Kellman A G, Kessel C E, Koslowski H R, LaHaye R J, Lazzaro E, Liu Y, Lukash V, Manickam J, Medvedev S, Mertens V, Mirnov S V, Nakamura Y, Navratil G A, Okabayashi M, Ozeki T, Paccagnella R, Pautasso G, Porcelli F, Pustovitov V D, Riccardo V, Sato M, Sauter O, Schaffer M J, Shimada M, Sonato P, Strait E J, Sugihara M, Takechi M, Turnbull A D, Westerhof E, Whyte D G, Yoshino R, Zohm H, Group, the Itpa Mhd D and Magnet 2007 *Nuclear Fusion* **47** S128–S202 ISSN 0029-5515 URL `http://stacks.iop.org/0029-5515/47/i=6/a=S03?key=crossref.0b9322e42a59b955269531e35f39b3bb`

[3] Lehnen M, Aleynikova K, Aleynikov P B, Campbell D J, Drewelow P, Eidietis N W, Gasparyan Y, Granetz R S, Gribov Y, Hartmann N, Hollmann E M, Izzo V A, Jachmich S, Kim S H, Kočan M, Koslowski H R, Kovalenko D, Kruezi U, Loarte A, Maruyama S, Matthews G F, Parks P B, Pautasso G, Pitts R A, Reux C, Riccardo V, Roccella R, Snipes J A, Thornton A J and de Vries P C 2015 *Journal of Nuclear Materials* **463** 39–48 ISSN 00223115 URL `http://linkinghub.elsevier.com/retrieve/pii/S0022311514007594`

[4] Hollmann E M, Aleynikov P B, Fülöp T, Humphreys D A, Izzo V A, Lehnen M, Lukash V E, Papp G, Pautasso G, Saint-Laurent F and Snipes J A 2015 *Physics of Plasmas* **22** 021802 ISSN 1070-664X URL `http://scitation.aip.org/content/aip/journal/pop/22/2/10.1063/1.4901251`

[5] Boozer A H 2015 *Physics of Plasmas* **22** ISSN 10897674 URL `http://dx.doi.org/10.1063/1.4913582`

[6] Papp G, Fülöp T, Fehér T, Vries P C D, Plyusnin V V, Alper B and Efda J E T 2013 *Nuclear Fusion* **53** 123017 ISSN 00295515

[7] Hollmann E M, Austin M E, Boedo J A, Brooks N H, Commaux N, Eidietis N W, Humphreys D A, Izzo V A, James A N, Jernigan T C, Loarte A, Martin-Solis J R, Moyer R A, Muñoz-Burgos J M, Parks P B, Rudakov D L, Strait E J, Tsui C, Van Zeeland M, Wesley J C and Yu J H 2013 *Nuclear Fusion* **53** 083004 ISSN 0029-5515 URL `http://stacks.iop.org/0029-5515/53/i=8/a=083004?key=crossref.57e075cb22a5f9e03d097378d8d1d788`

[8] Granetz R S, Esposito B, Kim J H, Koslowski H R, Lehnen M, Martin-Solis J R, Paz-Soldan C, Rhee T, Wesley J C, Zeng L and Group I M 2014 *Physics of Plasmas* **21** 072506 URL `http://dx.doi.org/10.1063/1.4886802`

[9] Reux C, Plyusnin V, Alper B, Alves D, Bazylev B and Belonohy E 2015 *Nuclear Fusion* **55** 093013

[10] Paz-Soldan C, Cooper C M, Aleynikov P B, Pace D C, Eidietis N W, Brennan D, Granetz R S, Hollmann E M, Liu C, Lvovskiy A, Moyer R A and Shiraki D 2017 *Physical Review Letters* **118** 255002 URL https://doi.org/10.1103/PhysRevLett.118.255002

[11] Esposito B, Boncagni L, Buratti P, Carnevale D, Causa F, Gospodarczyk M, Martin-Solis J R, Popovic Z, Agostini M, Apruzzese G, Bin W, Cianfarani C, De Angelis R, Granucci G, Grosso A, Maddaluno G, Marocco D, Piergotti V, Pensa A, Podda S, Pucella G, Ramogida G, Rocchi G, Riva M, Sibio A, Sozzi C, Tilia B, Tudisco O and Valisa M 2017 *Plasma Physics and Controlled Fusion* **59** 014044 ISSN 0741-3335 URL http://stacks.iop.org/0741-3335/59/i=1/a=014044?key=crossref.1e1c67020c21c6350db783fcc2bfa7c7

[12] Zeng L, Chen Z Y, Dong Y B, Koslowski H R, Liang Y, Zhang Y P, Zhuang H D, Huang D W and Gao X 2017 *Nuclear Fusion* **57** ISSN 17414326

[13] Shiraki D, Commaux N, Baylor L R, Cooper C M, Eidietis N W, Paz-Soldan C, Combs S K and Meitner S J 2018 *Nuclear Fusion* **58** 056006 URL https://doi.org/10.1088/1741-4326/aab0d6

[14] Shevelev A E, Khilkevitch E M and Kiptily V G 2018 *Nuclear Fusion* **58** 016034 URL http://iopscience.iop.org/article/10.1088/1741-4326/aa8cea/pdf

[15] Mlynar J, Ficker O, Macusova E, Markovic T, Naydenkova D, Papp G, Urban J, Vlainic M, Vondracek P, Weinzettl V, Bogar O, Bren D, Carnevale D, Casolari A, Cerovsky J, Farnik M, Gobbin M, Gospodarczyk M, Hron M, Kulhanek P, Havlicek J, Havranek A, Imrisek M, Jakubowski M, Lamas N, Linhart V, Malinowski K, Marcisovsky M, Matveeva E, Panek R, Plyusnin V V, Rabinski M, Svoboda V, Svihra P, Varju J, Zebrowski J, Team t C T and the EUROfusion MST1 2019 *Plasma Physics and Controlled Fusion* **61** 014010 ISSN 0741-3335 URL https://doi.org/10.1088/1361-6587/aae04a

[16] Carnevale D, Ariola M, Artaserse G, Bagnato F, Bin W, Boncagni L, Bolzonella T and Bombarda F 2019 *Plasma Physics and Controlled Fusion* **61** 014036 URL https://doi.org/10.1088/1361-6587/aaef53

[17] Freidberg J P 2014 *Ideal Magnetohydrodynamcis* 1st ed (Cambridge University Press) ISBN 978-1107006256

[18] Wesson J A 1987 *Tokamaks* 1st ed (Oxford: Oxford University Press) ISBN 0198563280

[19] Bateman G 1978 *Magnetohydrodynamic Instabilities* 1st ed (Boston, Massachussetts: The MIT Press) ISBN 0262021315

[20] Piovesan P, Hanson J M, Martin P A, Navratil G A, Turco F, Bialek J M, Ferraro N M, R, La Haye R J, Lanctot M J, Okabayashi M, Paz-Soldan C, Strait E J, Turnbull A D, Zanca P, Baruzzo M, Bolzonella T, Hyatt A W, Jackson G L, Marrelli L, Piron L and Shiraki D 2014 *Physical Review Letters* **113** 45003 URL http://link.aps.org/doi/10.1103/PhysRevLett.113.045003

[21] Turnbull A D, Ferraro N M, Hanson J M, Piovesan P and Martin P A 2016 *Journal of Plasma Physics* **83** 515820301

[22] Khayrutdinov R R and Lukash V E 1993 *Journal of Computational Physics* **109** 193–201 URL https://doi.org/10.1006/jcph.1993.1211

[23] Aleynikova K, Huijsmans G T A and Aleynikov P B 2016 *Plasma Physics Reports* **42** 486–494 ISSN 1063-780X URL http://link.springer.com/10.1134/S1063780X16050019

[24] Helander P, Grasso D, Hastie R J and Perona A 2007 *Physics of Plasmas* **14** 1–9 ISSN 1070664X URL http://dx.doi.org/10.1063/1.2817016

[25] Hollmann E M, Commaux N, Eidietis N W, Lasnier C J, Rudakov D L, Shiraki D, Cooper C M, Martin-Solis J R, Parks P B and Paz-Soldan C 2017 *Physics of Plasmas* **24** 062505 ISSN 1070-664X URL http://aip.scitation.org/doi/10.1063/1.4985086

[26] Boozer A H 2016 *Physics of Plasmas* **23** 082514 ISSN 10897674 URL https://doi.org/10.1063/1.4960969

[27] Boozer A H and Punjabi A 2016 *Physics of Plasmas* **23** 102513 ISSN 10897674 URL https://doi.org/10.1063/1.4966046

[28] Boozer A H 2017 *Nuclear Fusion* **57** 056018 ISSN 17414326 URL https://doi.org/10.1088/

1741-4326/aa6355

[29] Boozer A H 2018 *Nuclear Fusion* **58** 036006 ISSN 17414326 URL https://doi.org/10.1088/1741-4326/aaa1db

[30] Fülöp T, Smith H M and Pokol G I 2009 *Physics of Plasmas* **16** ISSN 1070664X

[31] Zeng L, Koslowski H R, Liang Y, Lvovskiy a, Lehnen M, Nicolai D, Pearson J, Rack M, Jaegers H, Finken K H, Wongrach K and Xu Y 2013 *Physical Review Letters* **110** 235003 ISSN 0031-9007 URL http://link.aps.org/doi/10.1103/PhysRevLett.110.235003

[32] Eidietis N W, Commaux N, Hollmann E M, Humphreys D A, Jernigan T C, Moyer R a, Strait E J, Van Zeeland M, Wesley J C and Yu J H 2012 *Physics of Plasmas* **19** 056109 ISSN 1070664X URL http://link.aip.org/link/PHPAEN/v19/i5/p056109/s1{&}Agg=doi

[33] Paz-Soldan C, Cooper C M, Aleynikov P B, Eidietis N W, Lvovskiy A, Pace D C, Brennan D, Hollmann E M, Liu C, Moyer R A and Shiraki D 2018 *Physics of Plasmas* **25** 056105 ISSN 1070-664X URL http://aip.scitation.org/doi/10.1063/1.5024223

[34] Liu C, Shi L, Hirvijoki E, Brennan D, Bhattacharjee A, Paz-Soldan C and Austin M E 2018 *Nuclear Fusion* **58** 096030 (*Preprint* 1803.09897) URL https://doi.org/10.1088/1741-4326/aacc9b

[35] King J D, Strait E J, Boivin R L, Taussig D, Watkins M G, Hanson J M, Logan N C, Paz-Soldan C, Shiraki D, Lanctot M J, La Haye R J, Lao L L, Battaglia D J, Sontag A C and Haskey S R 2014 *Review of Scientific Instruments* **85** 083503

[36] James A N, Austin M E, Commaux N, Eidietis N W, Evans T E, Hollmann E M, Humphreys D A, Hyatt A W, Izzo V A, Jernigan T C, La Haye R J, Parks P B, Strait E J, Tynan G R, Wesley J C and Yu J H 2012 *Nuclear Fusion* **52** 13007 URL http://stacks.iop.org/0029-5515/52/i=1/a=013007

[37] James A N, Hollmann E M and Tynan G R 2010 *Review of Scientific Instruments* **81** 10E306 ISSN 1089-7623 URL http://www.ncbi.nlm.nih.gov/pubmed/21034005

[38] Heidbrink W W 1986 *Review of Scientific Instruments* **57** 1769 ISSN 00346748 URL http://link.aip.org/link/RSINAK/v57/i8/p1769/s1{&}Agg=doi

[39] Hollmann E M, Parks P B, Commaux N, Eidietis N W, Moyer R A, Shiraki D, Austin M E, Lasnier C J, Paz-Soldan C and Rudakov D L 2015 *Physics of Plasmas* **22** 056108

[40] Lao L L, John H E S, Peng Q and Ferron J R 2005 *Fusion Science and Technology* **48** 968–977 URL https://doi.org/10.13182/FST48-968

[41] Humphreys D A and Kellman A G 1999 *Physics of Plasmas* **6** 2742 ISSN 1070664X URL http://scitation.aip.org/content/aip/journal/pop/6/7/10.1063/1.873231

[42] Lao L, John H S, Stambaugh R and Pfeiffer W 1985 *Nuclear Fusion* **25** 1421–1436 ISSN 0029-5515 URL http://stacks.iop.org/0029-5515/25/i=10/a=004?key=crossref.c65e30aa06f1625cee446eb0172b8e1a

[43] Loarte A, Riccardo V, Martin-Solis J R, Paley J, Huber A, Lehnen M and Contributors J E 2011 *Nuclear Fusion* **51** 73004 URL http://stacks.iop.org/0029-5515/51/i=7/a=073004

[44] Snipes J A, Campbell D J, Hugon M, Lomas P J, Nave M F, Haynes P S, Hender T C, Lopes Cardozo N J and Schüller F C 1988 *Nuclear Fusion* **28** 1085–1097 ISSN 17414326

[45] Cheng C Z, Furth H P and Boozer A H 1987 *Plasma Physics and Controlled Fusion* **29** 351–366 ISSN 07413335

[46] Martin-Solis J R, Loarte A and Lehnen M 2017 *Nuclear Fusion* **57** 066025 URL https://doi.org/10.1088/1741-4326/aa6939

[47] Eidietis N W, Gerhardt S P, Granetz R S, Kawano Y, Lehnen M, Lister J B, Pautasso G, Riccardo V, Tanna R L and Thornton A J 2015 *Nuclear Fusion* **55** ISSN 17414326

[48] Liu Y, Bondeson a, Fransson C M, Lennartson B and Breitholtz C 2000 *Physics of Plasmas* **7** 3681 ISSN 1070664X URL http://link.aip.org/link/PHPAEN/v7/i9/p3681/s1{&}Agg=doi

[49] Hollmann E M, Commaux N, Eidietis N W, Lasnier C J, Rudakov D L, Shiraki D, Cooper C M, Martin-Solis J R, Parks P B and Paz-Soldan C 2017 *Physics of Plasmas* **24** ISSN 10897674

[50] Northrop T G 1963 *Review of Geophysics* **1** 283–304 URL https://doi.org/10.1029/RG001i003p00283

[51] Callen J D, Hegna C C, Rice B W, Strait E J and Turnbull A D 1999 *Physics of Plasmas* **6** 2963–2967 URL http://link.aip.org/link/?PHP/6/2963/1